Journal of Sound and Vibration 535 (2022) 117069

Contents lists available at ScienceDirect

Journal of Sound and Vibration

journal homepage: www.elsevier.com/locate/jsvi

A dynamic disturbance force measurement system based on array sensor for large moving device in spacecrafts

Mingyi Xia [a,*], Chengbo Zhou [a,b], Enyang Zhang [a], Chunyang Han [a],
Zhenbang Xu [a,b,*]

[a] *Changchun Institute of Optics, Fine Mechanics and Physics, Chinese Academy of Science, Changchun, Jilin 130033, China*
[b] *Center of Materials Science and Optoelectronics Engineering, University of Chinese Academy of Sciences Beijing 100049,China*

ARTICLE INFO

Keywords:
Micro-vibration
Heavy load
Array sensor
D-optimal designs

ABSTRACT

The control of micro-vibrations is an increasingly significant aspect of the research related to high-precision equipment in spacecraft. As the scale and mass of these vibration sources become larger, the control precision required also increases, and the requirements for the vibration source ground test equipment are thus becoming more demanding. This paper therefore proposes a generalized disturbance force measurement system for large device vibration sources. The use of a redundant array of piezoelectric sensors can significantly increase the size, load capacity and stiffness of the platform. In addition, the D-optimal designs used by the system overcomes the redundant measurement errors introduced by array-based measurements. Based on the above, a more accurate 3D force decoupling expression is obtained using the linear decoupling algorithm of the full regression method. A system prototype is then designed and tested based on the results of this approach. Experimental results show that the system guarantees high load capacity (416 kN) and stiffness, the dynamic relative error within the 8–800 Hz frequency range is less than 3% for a 3D generalized force in the force hammer test, and the relative error of the test system under sinusoidal excitation is within 5%; additionally, the linearity for generalized forces over the full range is within 0.1% full scale and the results are not affected by the characteristics of the measured object.

1. Introduction

Space-based optical payloads have important applications in the fields of Earth observation and deep space exploration and their imaging performances are being improved continuously. The ground resolution of remote sensing satellites has been improved recently from tens of meters to less than 0.5 m [1–3]. In addition, ground observation resolution of less than 0.1 m has been achieved in military reconnaissance satellites. Deep space exploration resolution has changed from the 0.007″ achieved by the Hubble Space Telescope (HST) to the 0.004″ resolution of the James Webb Space Telescope (JWST) [4–7]. For China's large space telescope, the overall weight of the telescope may exceed 15,000 kg and the diameter of the main mirror is intended to be 2 m. The telescope's field of vision will be 300 times that of the HST. Because of its complex structure, this telescope will be more sensitive to micro-vibrations. Therefore, to study the effects of micro-vibrations on the telescope system, it will be necessary to study the disturbance

---

* Corresponding authors at: Changchun Institute of Optics, Fine Mechanics and Physics, Chinese Academy of Science, Changchun, Jilin 130033, China.

E-mail addresses: xiamingyi@ciomp.ac.cn (M. Xia), xuzhenbang@ciomp.ac.cn (Z. Xu).

https://doi.org/10.1016/j.jsv.2022.117069
Received 28 November 2021; Received in revised form 19 May 2022; Accepted 25 May 2022

mechanisms of the moving parts of the space telescope. Obviously, as the spacecraft becomes larger, its moving parts will also become larger; for example, in China's telescope, the output of a control moment gyroscope (CMG) is 500 Nm and its mass is 90 kg. After the installation equipment is added, the measurement platform will generally need to support loads of more than 1 ton (six CMGs) for the micro-vibration ground test [8–11]. In addition, the diameter of each functional module is close to 2 m, which requires a larger installation plane for fixing and measuring during acceptance. Therefore, the improvements in size and load capacity will be required in the ground measurement system. Based on the premise of ensuring high measurement precision and rigidity, it is difficult for existing measurement system designs to meet the heavy load measurement requirements described above.

Piezoelectric sensors have stronger abilities to bear heavy loads and also provide much greater robustness, which means that better performance is often provided in dynamic measurements with heavy loads of piezoelectric sensors [12–18]. Therefore, the current ground measurement systems for vibration sources mostly use piezoelectric systems. In the previous works [19–21] on piezoelectric measurement equipment, the Gough-Stewart platform was most commonly used, but its loose structure will reduce the rigidity of the platform significantly, which will limit the applicability of the Gough-Stewart platform for heavy load measurements. The orthogonal layout is mostly used by other platforms. For example, Li [22] designed a piezoelectric six-dimensional force measurement system for heavy loads that adopted a four-point redundant parallel configuration. However, the main intended purpose of this system was the static measurement of heavy loads without consideration of the effects of structural coupling. At the same time, the most commonly used Kistler-type multi-dimensional force measurement platform also adopted this type of layout. Xia [23] designed a novel generalized disturbance force measurement platform for large device vibration sources. The use of eight piezoelectric sensors at different positions allowed the structural stiffness of their platform to be improved. This system added four horizontal sensors on the basis of the four-point configuration, which belongs to a four-point-strengthened structure as a whole. Li [24] has also developed a parallel piezoelectric sensor for heavy load applications using a load-sharing approach. The load-bearing capacity of the test system was improved effectively through appropriate structural design of the load sharing ring. The performance of lead zirconate titanate (PZT) piezoelectric thick-film pressure sensors was investigated by Liang [25], and a unimorph sensor structure was fabricated. Durand [26] invented a measurement sensor for connecting wrenches, which consisted of six piezoelectric cylinders and were fixed in different orientations between two plates. Sujan [27] improved the maximum hysteresis characteristics and nonlinear performance of the sensor by designing a stainless steel resonant pressure sensor that can be used for piezoelectric excitation. Because of the characteristics of piezoelectric materials, the structure used is generally a parallel configuration similar to that described above.

Depending on the different working environments and test requirements, each of these measurement systems has a different structural design and different measurement principles that usually only require individual parameters to be designed. However, for the measurement requirements under high precision, heavy load and high rigidity conditions, the measurement principles above are likely to cause design conflicts. The main conflicts include the following: (1) Enlargement of the platform size will result in reduced stiffness and load capacity when using the traditional configuration. (2) To provide improved load capacity, it becomes necessary to strengthen the parallel link between the load platform and the base for load sharing. If the number of sensors is increased when using the traditional measurement strategy, unacceptable errors will be introduced. (3) Increasing the stiffness of the load platform will also affect the design of the system's load capacity [28]. Based on the investigations and research described above, it is necessary to find a balance and achieve coexistence among the various parameters.

This paper therefore proposes a measurement system based on a sensor array distribution and the corresponding measurement strategy. The design ideas are described here as follows. First, through use of an array of sensors and addition of parallel links, the upper limits for the platform size and the load capacity will be greatly increased. Second, based on use of the pre-vibration method, the mechanical characteristics of the measured vibration source will be understood. Third, via an optimization process to select the sensor set with the smallest error, the corresponding optimal measurement plan will be established for different vibration sources, thus improving the test precision. As a new test strategy, this paper only uses the three-dimensional (3D) generalized force measurement system for preliminary verification of the test results. Section 2 describes the basic design of the proposed system and establishes the decoupling error model. In Section 3, the operating principle and the optimization process for evaluation of the measured disturbance characteristics are analyzed theoretically, and a more precise formula for decoupling the forces is derived. Experiments are then

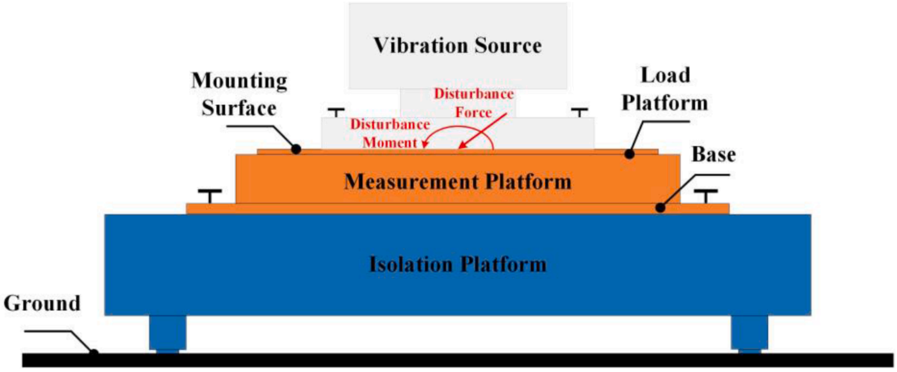

Fig. 1. Basic model of the measurement system.

performed to verify the dynamic mechanical properties of the proposed measurement system in Section 4. The conclusions from the study are then summarized in the final section.

2. Structure design and analysis

As shown in Fig. 1, different measurement systems can be described using the same basic model: a base, a load platform and sensors connecting the load platform to the base. The most important parameters for the proposed measurement system are the platform size, the load capacity, the structural stiffness and the measurement precision. These parameters often affect each other in terms of the measurement principle. To meet the effectiveness requirements of the various parameters for ground testing of large spacecraft, a new system is designed based on the traditional systems from the viewpoints of the platform structure and the measurement strategy.

2.1. Basic layout of the structure

Fig. 2 contains a schematic that illustrates the working principle of the array system prototype. This layout ensures that parameters such as the platform size, the platform rigidity and the load capacity have higher upper limits by connecting additional sensors in parallel between the load platform and the base. During measurement, the platform is fixed onto a vibration isolation platform through its base and the vibration source to be measured is mounted on the load platform. When the vibration source is operational, a disturbance force is transmitted to the sensors, which produce sufficient output signals to decouple the disturbance from the measured vibration source. By taking sufficient optimization space requirements and the existing test conditions into account, the prototype in this paper uses a basic layout composed of 4 × 4 sensors (9134B, Kistler; sensitivity: −3.8 pC/N; range: 26 kN; preload: 15–25 Nm), which can be used to solve for M_x, M_y and F_z (the force or moment in the directions of x, y and z).

Because the load capacity and the resolution of the system are mainly determined by the force sensor, the stiffness design of the prototype is considered via finite element analysis (FEA). Structural coupling characteristics are required in the system in this paper to increase the optimization space [29,30]. For this reason, the load platform and base are made from thin plates with relatively low rigidity. The FEA model, which is based on MSC Nastran, is shown in Fig. 3(a). The model uses a 1/4 symmetry modeling method. The main element type is the hexahedral element (99.53%), the number of nodes is 10,531, the number of elements is 6803, and the number of MPCs (multipoint constraints) is 0. The components are connected by node coupling. From the MSC Nastran results, the fundamental frequency is 1173.1 Hz and the second-order natural frequency is 1227 Hz which are not in the frequency range of interest 8–800 Hz. This fundamental frequency can cause weak structural coupling and meets the rigidity requirements of the platform. The same method was used for the FEA of the platform with 2 × 2 sensors. It can be observed from Fig. 3(b) that the fundamental frequency is 362.7 Hz and the second-order frequency is 646.5 Hz. From the above comparison, it can be found that the platform with 4 × 4 sensors has better stiffness, which means that its load capacity has been greatly enhanced. Additionally when compared with the traditional configuration, the rigidity design of the proposed array layout is simpler and the design requirements for the load platform in particular are reduced. The system rigidity achieved through FEA has a high upper limit, which is the advantage produced by increasing the number of sensors used, but this also has a significant effect on the test precision.

2.2. Decoupling error for redundant sensors

Increasing the number of sensors used in connecting can improve both the stiffness and the load capacity of the system effectively. However, excessive redundant sensors may cause serious system errors when the calibration matrix is decoupled. The relevant theory is studied by Xia [23], as shown in Eq. (1):

$$\varepsilon_a = 3\varepsilon_F + \varepsilon_V \tag{1}$$

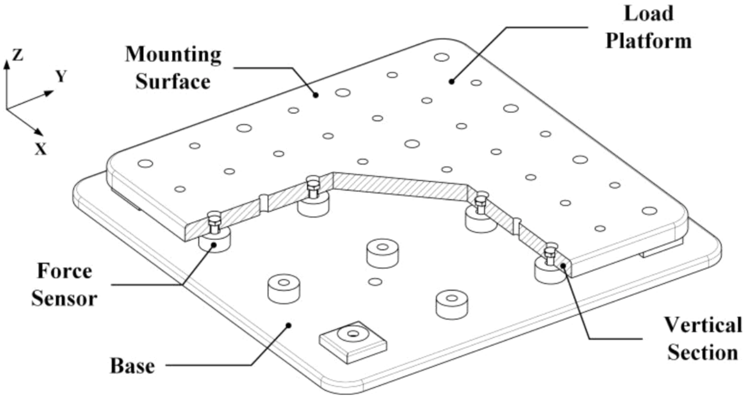

Fig. 2. Basic structure of the array measurement system (not only limited to 4 × 4 sensors).

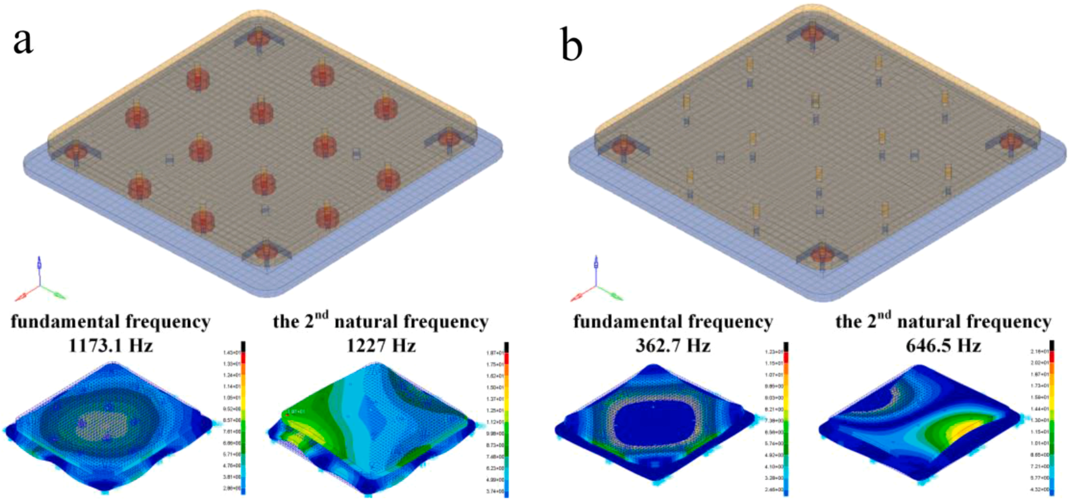

Fig. 3. Finite element models and cloud charts showing the first two order modes of two systems: (a) system with 4 × 4 sensors; (b) system with 2 × 2 sensors.

where ε_a, ε_V and ε_F are, respectively the relative error of the sensor calibration, the relative error of the measurement output V, and the relative error of the calibration force F. When the number of calibrated force vectors n satisfies the condition that $n>6$, the relative error associated with the calibration force matrix is amplified compared to $n = 6$. This indicates that system error magnification occurs due to redundant calibration. A similar conclusion will be obtained if the number of sensors is changed though a similar derivation in the Xia's paper, i.e., redundant decoupling (redundant observation and calibration) will also cause significant amplification of the system error [31–33]. However, more random components are included in the environmental error and thus increasing the number of participating sensors can also improve the test precision effectively. Therefore, to improve the actual test precision, it is necessary to evaluate both the environmental noise and the characteristics of the measured object and then optimize the test strategy based on the results of this pre-vibration evaluation. Traditional measurement schemes cannot be optimized because of the system packaging. However, in systems with an array layout that contain sufficient numbers of sensors, it becomes feasible to use different measurement methods for the different vibration sources. This paper provides a method for selecting the appropriate sensor combination, to improve system test precision under the premise of ensuring that it has the required structural characteristics (i.e., its platform size, rigidity, and load capacity).

3. Disturbance force decoupling and optimal strategy

In an actual measurement process, the composition of the environmental noise, the mass and disturbance characteristics of the measured vibration source, and the mechanical processing and assembly errors of the system are all random variables. The sensitivity

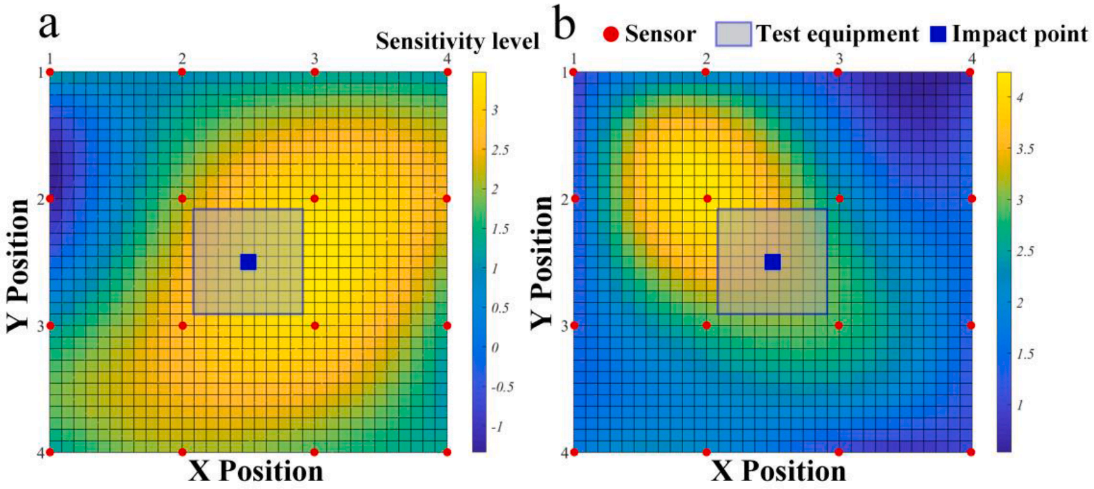

Fig. 4. Cloud chart showing sensitivity of sensors for F_z input: (a) time-domain maximum value; (b) frequency-domain RMS.

of the system's internal sensors to the measured vibration source therefore cannot be predicted.

When a vertical impact force is loaded at different points on the load platform of the prototype, the responses of each sensor are as shown in Figs. 4 and 5, which include the time-domain maximum value and the frequency-domain root mean square (RMS) statistics; while the maximum value provides more of a reflection of the transient response characteristics, the RMS results reflect the broadband response characteristics. The cloud image is generated via secondary polynomial fitting based on the real data for each point. Fig. 4 shows the results obtained when the load is at the center position. Theoretically, the response of each sensor should be the same; in reality, however, because of the effects of the random variables mentioned above, the responses of each sensor show obvious concentrations. This is inevitable in actual tests, particularly for measurements of different vibration sources. Fig. 5 shows the results when the load is at the edge position. The sensor responses far away from the loading point are very small and are close to the environmental noise level, and are thus more susceptible to environmental effects. After decoupling using the calibration matrix, the errors will be amplified to different degrees. Therefore, depending on the different disturbance sources, the disturbance characteristics and the system response must be evaluated based on the pre-vibration results, and a high precision test strategy can then be constructed that will improve the test precision effectively. So the key to the current problem can be summarized as how many sensors are selected for decoupling, how decoupling is performed, and where the sensors are located.

3.1. *Environmental noise evaluation*

To evaluate the disturbance characteristics, it is necessary to pre-vibrate the measured vibration source in a manner similar to the principle of a vibration simulation system. The response signal of each sensor is then obtained by starting the measured vibration source or external excitation.

First, the composition of the environmental noise must be evaluated to determine the number of sensors required to decouple the measured vibration source. Therefore, the coherence function is evaluated with reference to Eq. (2) to quantize the environmental noise.

$$\gamma^2 = \frac{\left|G_{fx}(\omega)\right|^2}{G_{ff}(\omega)G_{xx}(\omega)} \tag{2}$$

where $G_{fx}(\omega)$, $G_{ff}(\omega)$ and $G_{xx}(\omega)$ are, respectively the mutual spectrum of input and output signals, the self-spectrum of the output signal and the self-spectrum of the input signal, and the power spectra can be calculated when the input and output signals are obtained. Coherence function satisfies the following conditions:

$$0 \le \gamma^2 \le 1 \tag{3}$$

When $\gamma^2 = 1$, the test signal is completely free from noise pollution; when $\gamma^2 = 0$, the test signal is totally drowned by noise. Therefore, the coherence function is used to evaluate whether or not the random error component of the signal meets the conventional test conditions to determine if the process is redundant observation with the number of sensors $m>6$ or non-redundant observation with $m = 6$ (only 3D generalized forces are considered in this prototype and thus $m = 3$). This measurement strategy is intended to reduce the random errors by increasing the number of participating sensors, but to prevent introduction of systematic errors, non-redundant observation methods should be used when the environment is suitable.

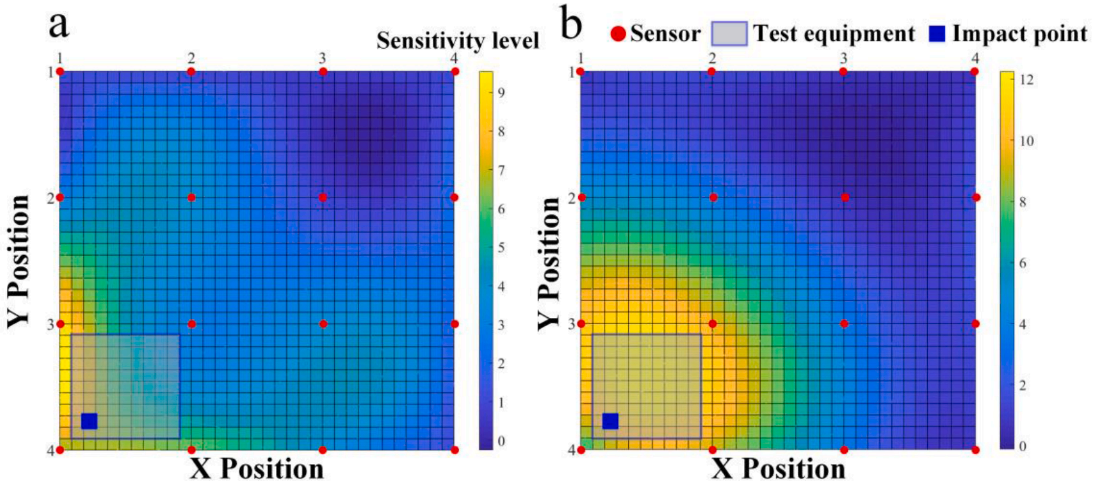

Fig. 5. Cloud chart showing sensitivity of sensors for F_z and M_x and M_y input: (a) time-domain maximum value; (b) frequency-domain RMS.

3.2. Decoupling of disturbance forces

Second, once the number of sensors m has been determined, the decoupling of the disturbance forces will be carried out. Because the amplitude and frequency of micro-vibrations are distributed widely, the micro-vibration measurement and decoupling in this paper are based on spectral analysis.

Let $F(t_k)$ and $U_i(t_k)$ be the time domain input signals and the output signals of the 16 sensors, respectively, where i means the ith sensor channel and t_k is the sampling moment. The input signal $F(\omega)$ and the response signal $U_i(\omega)$ of the 16-way sensor in the frequency domain can be obtained from the discrete Fourier transform equation:

$$X(\omega_n) = \mathrm{DFT}\left\{x(t_k)\right\} = \sum_{k=0}^{N-1} x(t_k) e^{-\mathrm{j}2\pi kn/N} \tag{4}$$

Then the output signals of m sensors are arbitrarily selected for 3D force decoupling. There are numerous methods can be used for 3D force decoupling. The decoupling algorithm based on the generalized inverse solution of matrices is used to decouple 3D force and get the optimal channel group considering the economy of computer resources during calculation and the superiority of Matlab in solving matrices.

The vector $\mathbf{F}(\omega) = [M_x(\omega)\ M_y(\omega)\ F_z(\omega)]^{\mathrm{T}}$ is used to represent the force input signal, and $\mathbf{U}(\omega)=[U_1(\omega)\ U_2(\omega)\ \dots\ U_m(\omega)]^{\mathrm{T}}$ represents the voltage output signal, and $\mathbf{B}(\omega)$ is the constant error matrix, then the relationship between the force and voltage is shown in Eq. (5):

$$\begin{bmatrix} U1(\omega) \\ U2(\omega) \\ U3(\omega) \\ \vdots \\ Um(\omega) \end{bmatrix} = \begin{bmatrix} V11(\omega) & V21(\omega) & V31(\omega) \\ V12(\omega) & V22(\omega) & V32(\omega) \\ V13(\omega) & V23(\omega) & V33(\omega) \\ \vdots & \vdots & \vdots \\ V1m(\omega) & V2m(\omega) & V3m(\omega) \end{bmatrix} \begin{bmatrix} M_x(\omega) \\ M_y(\omega) \\ F_z(\omega) \end{bmatrix} + \mathbf{B}(\omega) \tag{5}$$

The Eq. (5) can be written as Eq. (6):

$$\mathbf{U}(\omega) = \mathbf{V}(\omega)\mathbf{F}(\omega) + \mathbf{B}(\omega) \tag{6}$$

The calibration matrix $\mathbf{V}(\omega)$ can be obtained by means of the generalized inverse of the matrix in order to minimize the index $J = \mathbf{B}(\omega)^{\mathrm{T}}\mathbf{B}(\omega)$.

$$\widetilde{\mathbf{V}}(\omega) = \mathbf{U}(\omega)\mathbf{F}(\omega)^{\mathrm{T}}\left(\mathbf{F}(\omega)\mathbf{F}(\omega)^{\mathrm{T}}\right)^{-1} \tag{7}$$

Substituting Eq. (7) into Eq. (6), the calculation gives a least squares estimate of $\mathbf{F}(\omega)$:

$$\widetilde{\mathbf{F}}(\omega) = \left(\widetilde{\mathbf{V}}(\omega)^{\mathrm{T}}\widetilde{\mathbf{V}}(\omega)\right)^{-1}\widetilde{\mathbf{V}}(\omega)^{\mathrm{T}}\mathbf{U}(\omega) \tag{8}$$

The decoupling of the three-dimensional forces is now completed.

3.3. Optimization algorithm

There are 16 sensors that can be selected for the solution of Eqs. (7) and (8). What will be discussed is which m sensors can form the optimal sensor set so that the decoupling produces the least error. Define $\widetilde{\mathbf{V}}\mathrm{cs}(\omega)$ to be a subset of 16 sensors containing columns corresponding to m sensors selected. $\widetilde{\mathbf{V}}\mathrm{cs}(\omega)$ is called the candidate set. With respect to a randomly selected subset, the approximate solution to Eq. (8) can be expressed as:

$$\widetilde{\mathbf{F}}(\omega) \cong \widehat{\mathbf{F}}(\omega) = \left(\widetilde{\mathbf{V}}\mathrm{cs}(\omega)^{\mathrm{T}}\widetilde{\mathbf{V}}\mathrm{cs}(\omega)\right)^{-1}\widetilde{\mathbf{V}}\mathrm{cs}(\omega)^{\mathrm{T}}\mathbf{U}(\omega) \tag{9}$$

However Eq. (9) suffers from ill-conditioning. $\mathbf{U}(\omega)$ is prone to measuring errors practically and being ill-conditioned often occurs in the inverse problem identified by Eq. (9). Small variation (e.g. noise) in $\mathbf{U}(\omega)$ can lead to a large error in the estimation of $\widehat{\mathbf{F}}(\omega)$. The accuracy of $\widehat{\mathbf{F}}(\omega)$ relies on choice of sensors' positions. The crucial question is how to find the optimal $\widetilde{\mathbf{V}}\mathrm{cs}(\omega)$.

If the errors in output measurements are statistically independent and the standard deviation of one is σ, then the covariance matrix for $\widehat{\mathbf{F}}(\omega)$ can be given by Eq. (10):

$$\mathrm{var}\left(\widehat{\mathbf{F}}(\omega)\right) = \sigma^2\left(\widetilde{\mathbf{V}}\mathrm{cs}(\omega)^{\mathrm{T}}\widetilde{\mathbf{V}}\mathrm{cs}(\omega)\right)^{-1} \tag{10}$$

where $\left(\widetilde{\mathbf{V}}\mathrm{cs}(\omega)^{\mathrm{T}}\widetilde{\mathbf{V}}\mathrm{cs}(\omega)\right)^{-1}$ is known as the sensitivity of $\widetilde{\mathbf{V}}\mathrm{cs}(\omega)$. When σ^2 is certain, minimizing the sensitivity of $\widetilde{\mathbf{V}}\mathrm{cs}(\omega)$ will improve the accuracy of $\widehat{\mathbf{F}}(\omega)$. Consequently, optimum selection of the locations of sensors can minimize the sensitivity of $\widetilde{\mathbf{V}}\mathrm{cs}(\omega)$.

For a given number of sensors 16, the optimal $\widetilde{\mathbf{V}}\mathrm{cs}(\omega)$ is searched to determine a sensors locations that provide the least variance in the force estimation. It is key to find the optimal combination of sensors to maximize $|\widetilde{\mathbf{V}}\mathrm{cs}(\omega)^{\mathrm{T}}\widetilde{\mathbf{V}}\mathrm{cs}(\omega)|$ where $\widetilde{\mathbf{V}}\mathrm{cs}(\omega)$ is obtained by Eq. (7) using m sets of output data $\mathbf{U}(\omega)$. Designs maximizing $|\widetilde{\mathbf{V}}\mathrm{cs}(\omega)^{\mathrm{T}}\widetilde{\mathbf{V}}\mathrm{cs}(\omega)|$ is called D-optimal designs where D indicates determinant [34–36]. In this paper, sequential exchange algorithms are used.

The m sensors from the 16 are selected randomly, then substitute the output data into Eq. (7) to initialize $\widetilde{\mathbf{V}}\mathrm{cs}(\omega)$. Out of the remaining sensors, one sensor is then selected. Among these $m+1$ sensors, the m sensors are chosen to make $|\widetilde{\mathbf{V}}\mathrm{cs}(\omega)^{\mathrm{T}}\widetilde{\mathbf{V}}\mathrm{cs}(\omega)|$ maximum and the remaining one should be deleted. This process of selecting and deleting sensors continues until here is no further improvement in the value of $|\widetilde{\mathbf{V}}\mathrm{cs}(\omega)^{\mathrm{T}}\widetilde{\mathbf{V}}\mathrm{cs}(\omega)|$. The final $\widetilde{\mathbf{V}}\mathrm{cs}(\omega)$ is the D-optimal design $\mathbf{V}_{\mathrm{opt}}(\omega)$, then the optimal sensor combination by $\mathbf{V}_{\mathrm{opt}}(\omega)$ can be get. Once $\mathbf{V}_{\mathrm{opt}}(\omega)$ and, in turn, the optimal sensor combination are determined, $\mathbf{U}_{\mathrm{opt}}(\omega)$ can also be obtained. $\widehat{\mathbf{F}}(\omega)$, which is an approximation to $\widetilde{\mathbf{F}}(\omega)$, is then estimated using the deterministic form of Eq. (9) as:

$$\widetilde{\mathbf{F}}(\omega)\cong\widehat{\mathbf{F}}(\omega)=\left(\mathbf{V}_{\mathrm{opt}}(\omega)^{\mathrm{T}}\mathbf{V}_{\mathrm{opt}}(\omega)\right)^{-1}\mathbf{V}_{\mathrm{opt}}(\omega)^{\mathrm{T}}\mathbf{U}_{\mathrm{opt}}(\omega) \tag{11}$$

The process of D optimization is shown in Fig. 6.

3.4. Improvement of force decoupling

Although the above method decouples the 3D forces in a less computationally complex, less time-consuming and faster way, but the calculation decoupling forces by finding the generalized inverse matrix does not take the bias value into account when the voltage matrix is zero, which makes the solution to certain errors.

The optimal sensor combination must be obtained through the analysis in the previous subsection, then the corresponding output data need to be selected for a more accurate 3D force decoupling calculation. $m\times h$ sets of data from m sensors (each sensor can get h sets of data by tapping h different points) are chosen to be used for linear decoupling based on full regression method.

Assume that the output data of the optimal sensors are $U_{1k}(\omega)$, $U_{2k}(\omega)$, …, $U_{mk}(\omega)$, where m represents the number of selected sensors and $k=1,2,\ldots,h$ implies the location of each input of force. Similarly, the input forces were measured with h sets. Let the linear relationship between the force $F_z(\omega)$ in the z-direction and the voltage values $U_1(\omega)$, $U_2(\omega)$, …, $U_m(\omega)$ of the m optimal channels be as in Eq. (12):

$$F_z(\omega)=\beta_0(\omega)+\beta_1(\omega)U_1(\omega)+\beta_2(\omega)U_2(\omega)+\cdots+\beta_m(\omega)U_m(\omega)+\varepsilon(\omega) \tag{12}$$

Eq. (12) is the regression equation, where $\beta_0(\omega)$, $\beta_1(\omega)$, $\beta_2(\omega)$, …, $\beta_m(\omega)$ are the regression coefficients and $\varepsilon(\omega)$ is the residual error. The regression coefficients can be calculated from the h sets of test data. Substitute test data into Eq. (12):

$$F_{zk}(\omega)=\beta_0(\omega)+\beta_1(\omega)U_{1k}(\omega)+\beta_2(\omega)U_{2k}(\omega)+\cdots+\beta_m(\omega)U_{mk}(\omega)+\varepsilon_k(\omega) \tag{13}$$

where $\varepsilon_k(\omega)$ is the error of each test. Let the estimate of $\beta_i(\omega)$ $(i=0,1,2,\ldots,m)$ be $b_i(\omega)$ and the estimate of $\varepsilon_k(\omega)$ be $e_k(\omega)$. Eq. (13) can be rewritten as Eq. (14):

$$F_{zk}(\omega)=b_0(\omega)+b_1(\omega)U_{1k}(\omega)+b_2(\omega)U_{2k}(\omega)+\cdots+b_m(\omega)U_{mk}(\omega)+e_k(\omega) \tag{14}$$

Let the valuation of $F_{zk}(\omega)$ be $\widehat{F}_{zk}(\omega)$as shown in Eq. (15).

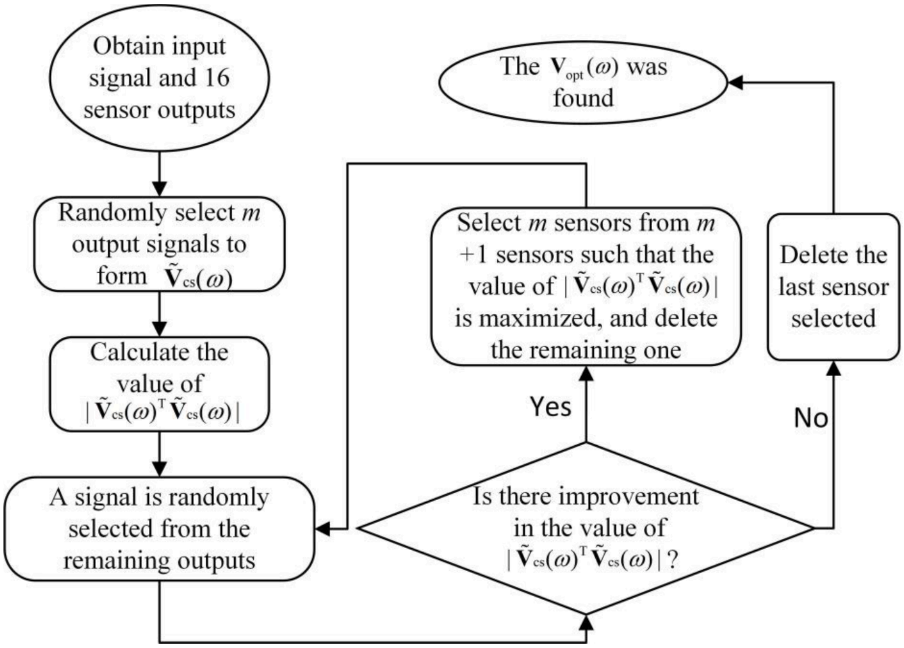

Fig. 6. The process of D optimization.

$$\widehat{F}_{zk}(\omega) = b_0(\omega) + b_1(\omega)U_{1k}(\omega) + b_2(\omega)U_{2k}(\omega) + \cdots + b_m(\omega)U_{mk}(\omega) \tag{15}$$

Combining Eqs. (14) and (15) yields $e_k(\omega)$:

$$\begin{gathered} e_k(\omega) = F_{zk}(\omega) - \widehat{F}_{zk}(\omega) \\ = F_{zk}(\omega) - (b_0(\omega) + b_1(\omega)U_{1k}(\omega) + b_2(\omega)U_{2k}(\omega) + \cdots + b_m(\omega)U_{mk}(\omega)) \end{gathered} \tag{16}$$

The values of each $b_i(\omega)$ can be found by least squares method that minimizes the sum of squares of residuals $e_k(\omega)$.

$$Q = \sum_{k=1}^{h} {e_k}^2(\omega) = \sum_{k=1}^{h} [F_{zk}(\omega) - \widehat{F}_{zk}(\omega)]^2 \tag{17}$$

From the extreme value principle, it follows that $b_i(\omega)$ must satisfy that the partial derivatives of Q with respect to each $b_i(\omega)$ are 0 if Q is to be minimized.

$$\frac{\partial Q}{\partial b_i(\omega)} = 0 \ (i = 1, 2, \cdots, m) \tag{18}$$

Eq. (19) can be deduced from Eq. (18):

$$\sum_{k=1}^{h} [F_{zk}(\omega) - (b_0(\omega) + b_1(\omega)U_{1k}(\omega) + b_2(\omega)U_{2k}(\omega) + \cdots + b_m(\omega)U_{mk}(\omega))] = 0 \tag{19}$$

The average value of each test data is shown in Eqs. (20) and (21):

$$\overline{U}_i(\omega) = \frac{1}{h}\sum_{k=1}^{h} U_{ik}(\omega) \ (i = 1, 2, \cdots, m) \tag{20}$$

$$\overline{F}_z(\omega) = \frac{1}{h}\sum_{k=1}^{h} F_{zk}(\omega) \tag{21}$$

Substituting Eqs. (20) and (21) into Eq. (17) yields b_0 as shown in Eq. (22):

$$b_0(\omega) = \overline{F}_z - \sum_{i=1}^{m} b_i(\omega)\overline{U}_i(\omega) \tag{22}$$

To facilitate the calculation of Eq. (22), the variables $U_{ik}(\omega)$ and $F_{zk}(\omega)$ can be written in the form of deviations from the mean of the measured data, respectively:

$$U'_{ik} = U_{ik}(\omega) - \overline{U}_i(\omega) \ (i = 1, 2, \cdots, m) \tag{23}$$

$$F'_{zk} = F_{zk}(\omega) - \overline{F}_z(\omega) \tag{24}$$

Eqs. (25)–(27) Can be easily obtained by substituting Eqs. (23) and (24) into Eqs. (15)–(17).

$$\widehat{F}_{zk}(\omega) = \overline{F}_z + \left[b_1(\omega)U'_{1k}(\omega) + b_2(\omega)U'_{2k}(\omega) + \cdots + b_m(\omega)U'_{mk}(\omega)\right] \tag{25}$$

$$\begin{gathered} e_k(\omega) = F_{zk}(\omega) - \widehat{F}_{zk}(\omega) \\ = F'_{zk} - \left[b_1(\omega)U'_{1k}(\omega) + b_2(\omega)U'_{2k}(\omega) + \cdots + b_m(\omega)U'_{mk}(\omega)\right] \end{gathered} \tag{26}$$

$$Q = \sum_{k=1}^{h} {e_k}^2(\omega) \tag{27}$$

Eq. (18) can be written as Eq. (28):

$$\begin{gathered} -\frac{\partial Q}{2\partial b1} = \sum_{k=1}^{h} \left[F'_{zk}(\omega) - (b_1(\omega)U'_{1k}(\omega) + \cdots + b_m(\omega)U'_{mk}(\omega))\right] U'_{1k}(\omega) = 0 \\ -\frac{\partial Q}{2\partial b2} = \sum_{k=1}^{h} \left[F'_{zk}(\omega) - (b_1(\omega)U'_{1k}(\omega) + \cdots + b_m(\omega)U'_{mk}(\omega))\right] U'_{2k}(\omega) = 0 \\ \vdots \\ -\frac{\partial Q}{2\partial bm} = \sum_{k=1}^{h} \left[F'_{zk}(\omega) - (b_1(\omega)U'_{1k}(\omega) + \cdots + b_m(\omega)U'_{mk}(\omega))\right] U'_{mk}(\omega) = 0 \end{gathered} \tag{28}$$

Writing the above equation in the form of a matrix yields Eq. (29).

$$\begin{bmatrix} b1(\omega) \\ b2(\omega) \\ \vdots \\ bm(\omega) \end{bmatrix}^{\mathrm{T}} \begin{bmatrix} S11(\omega) & S21(\omega) & \cdots & Sm1(\omega) \\ S12(\omega) & S22(\omega) & \cdots & Sm2(\omega) \\ \vdots & \vdots & \ddots & \vdots \\ S1m(\omega) & S2m(\omega) & \cdots & Smm(\omega) \end{bmatrix} = \begin{bmatrix} S1y(\omega) \\ S2y(\omega) \\ \vdots \\ Smy(\omega) \end{bmatrix}^{\mathrm{T}} \tag{29}$$

where $\boldsymbol{Sij}(\omega) = \sum_{k=1}^{h} U'_{ik}(\omega)U'_{jk}(\omega)$, $\boldsymbol{Siy}(\omega) = \sum_{k=1}^{h} F'_{zk}(\omega)U'_{ik}(\omega)$.

The specific expression of Eq. (15) can be obtained from the above calculation. Similarly, the expressions of $M_x(\omega)$ and $M_y(\omega)$ with respect to $U_1(\omega)$, $U_2(\omega)$, …, $U_m(\omega)$ can be derived, respectively. If the expression of the signal in the time domain can be got, the force signal in the frequency domain can be substituted into Eq. (30):

$$x(t_k) = \mathrm{IDFT}\{X(\omega_n)\}\Big\} = \frac{1}{N}\sum_{k=0}^{N-1} X(\omega_n)e^{-\mathrm{j}2\pi kn/N} \tag{30}$$

From the above analysis, the optimal combination of sensors from 16 sensors and decoupled the three-dimensional forces can be acquired.

4. Experimental verification

Experimental section mainly includes verification of the rigidity and the dynamic linearity of the array measurement system prototype; verification of the selection of optimal sensor combinations for vibration experiments and the process of solving three-dimensional force expressions, i.e., pre-vibration experiments; completion of the disturbance force testing, detection of the dynamic force measurement precision, and verification of the theories above [23].

4.1. *Dynamic mechanical performance test*

Fig. 7 shows the dynamic mechanical performance test system, the system includes system prototype, loading equipment, charge amplifier, a data acquisition device (precision: ±0.1 dB; VRAI820–24bit, $M + P$, Germany), PC and an impact hammer (086C03, PCB; sensitivity: 2.25 mV/N; resolution: 0.02 N-rms; range: ±2200 N-pk.).

The distribution of the sensors of the force measurement platform is shown in Fig. 8. No sensors are arranged on the axis, thus ensuring that any m sensors can be decoupled from the 3D generalized force. Where, $a_1 = b_1 = 0.15$ m, $a_{11} = b_{11} = 0.05$ m.

In order to verify the dynamic linearity, the broadband impact of different amplitudes are input through loading equipment and the FRF (frequency response function) curves of each sensor are detected. It can be seen from the FRF curve as shown in Fig. 9 that the fundamental frequency of the system is 1174 Hz at a sampling frequency of 8192 Hz (the bandwidth is 0.0625 Hz–3200 Hz, the effective coefficient is 2.56). The simulated result was 1173.1 Hz. These two values are extremely close that even the simulation model does not need to be modified, which also shows the advantage in stiffness simulation for the array measurement system. In order to provide sufficient space for the improvement of structural stiffness, the load platform is designed to be thin plate. By strengthening the load platform and base, the fundamental frequency of array system can be easily increased.

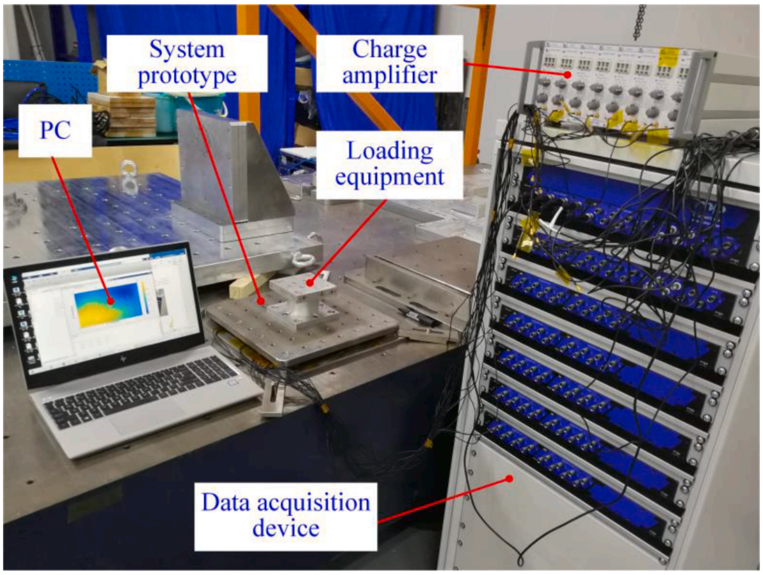

Fig. 7. Dynamic mechanical performance test system.

And the relative error between the FRF curves can be used to characterize the dynamic linearity as shown in Fig. 9. The results show that the dynamic linearity of each sensor can be guaranteed within 0.1% full scale, but it is affected by the power frequency (50 Hz and its harmonics) in the red square of Fig. 9(b). Comparing the sensor response of position 6 and position 9, after filtering the FRF curves has a translation, which is introduced by the existing bad test environment, which is difficult to avoid during the micro-vibration test.

4.2. *Pre-vibration experiment*

As shown in Fig. 10, loading equipment is mounted on the platform at the position 2–7 (the diagonal of mounting position are sensor 2 and 7). There are nine loading points on the loading equipment, and impact force can be applied to the points of loading equipment (see in Fig. 11) using the hammer.

This experiment takes point 1, 5, and 9 to input the broadband impact force. Each point was loaded three times, and the average values of the hammer and sensor signals can be used as the measured data to reduce the effects of random errors. The frequency domain response curve of the system and the FRF curve can be both produced using a data sampling frequency of 2048 Hz, and a sampling time of 16 s. The length of each element $V_{ij}(\omega)$ of the calibration matrix is 32,768, which has an effective bandwidth of 1/16–800 Hz (the effective coefficient of $\mathbf{V}(\omega)$ is 2.56.).

The non-redundant observation with a sensor number of 3 ($m = 3$) is chosen by the calculation of the coherence function by Eq. (2). It can be considered that there is little interference from the environment when the value of the coherence function is greater than 0.8, and the green line in the Fig. 12 is the labeled line of the coherence function equal to 0.8. From the coherence function plot in Fig. 12, it can be known that the noise of the environment interferes little with the experiment (because of the bad low frequency characteristics of piezoelectric ceramics, it is acceptable that the coherence function is poor at low frequencies).

The input signal and response signal in the frequency domain are obtained by Eq. (4). Since the applied load is not on the mounting surface of platform, the calibration forces need to be converted into equivalent forces that act on the center O of the mounting surface, i.e.,

$$\mathbf{F}(\omega) = \mathbf{C}\mathbf{F}'(\omega) \tag{31}$$

where $\mathbf{F}(\omega)$ denotes the load equivalent to the center of the platform mounting surface, and $\mathbf{F}'(\omega)$ is the calibration forces. From the installation position 2–7 of the loading equipment, $\mathbf{C}$ can be obtained as:

$$\mathbf{C} = \begin{bmatrix} -0.15 & -0.10 & -0.05 \\ -0.05 & 0 & 0.05 \\ 1 & 1 & 1 \end{bmatrix} \tag{32}$$

Therefore, Eq. (5) can be rewritten as:

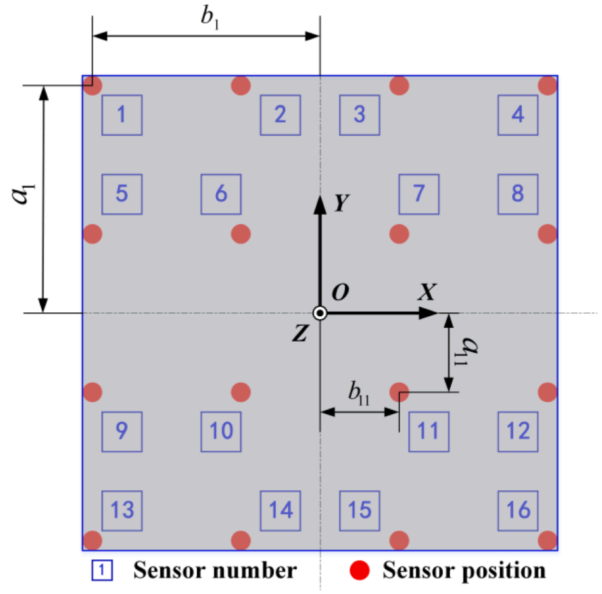

Fig. 8. Distribution position parameters of the sensors.

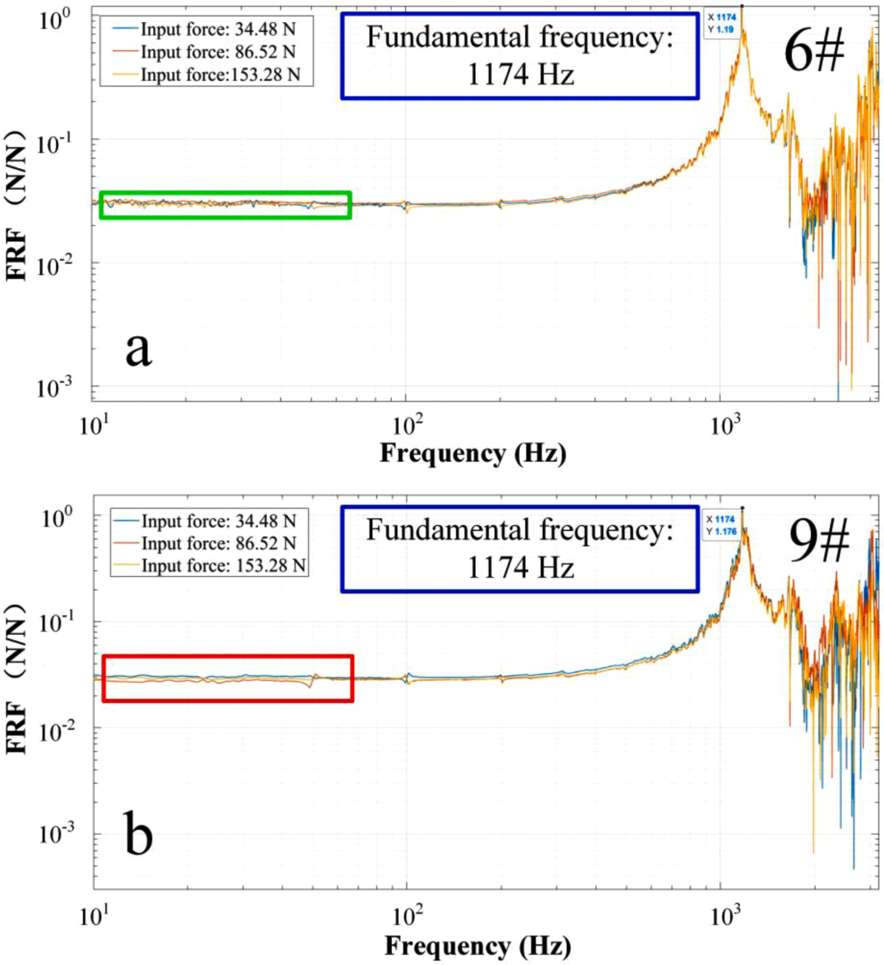

Fig. 9. Frequency response function curve of the system: (a) Sensor of position 6; (b) Sensor of position 9.

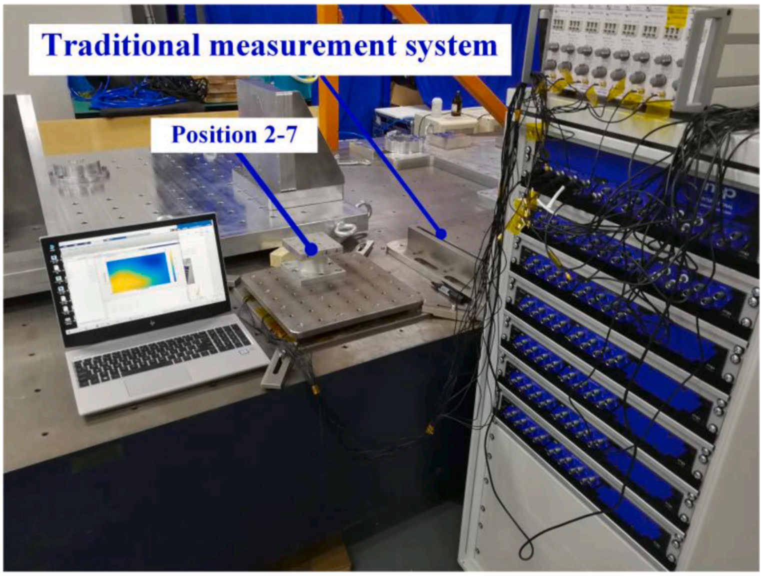

Fig. 10. Test system and equipment position 2–7.

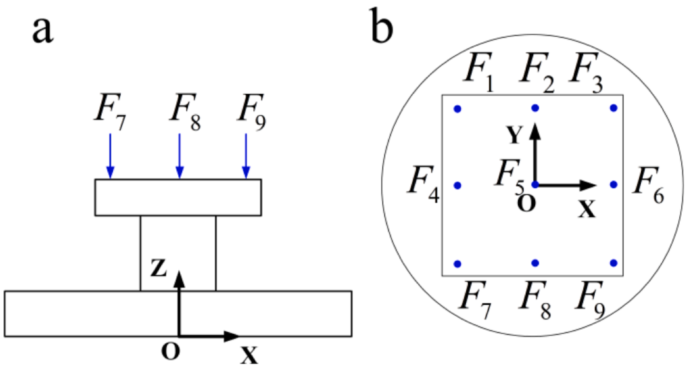

Fig. 11. Layout of the load points for the calibration process: (a) Front view; (b) Top view.

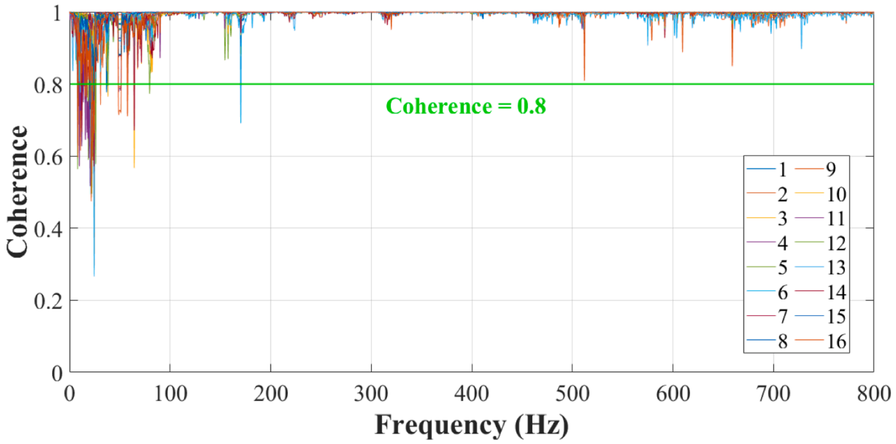

Fig. 12. Coherence function plot (Frequency range:8–800 Hz).

$$\begin{bmatrix} U11(\omega) & U15(\omega) & U19(\omega) \\ U21(\omega) & U25(\omega) & U29(\omega) \\ U31(\omega) & U35(\omega) & U39(\omega) \end{bmatrix} = \begin{bmatrix} V11(\omega) & V12(\omega) & V13(\omega) \\ V21(\omega) & V22(\omega) & V23(\omega) \\ V31(\omega) & V32(\omega) & V33(\omega) \end{bmatrix} \begin{bmatrix} -0.15 & -0.10 & -0.05 \\ -0.05 & 0 & 0.05 \\ 1 & 1 & 1 \end{bmatrix} \begin{bmatrix} F1(\omega) & 0 & 0 \\ 0 & F_5(\omega) & 0 \\ 0 & 0 & F_9(\omega) \end{bmatrix} + \mathbf{B}(\omega) \tag{33}$$

where $F_1(\omega)$, $F_5(\omega)$, and $F_9(\omega)$ represent the input forces through points 1, 5, and 9 and $U_{i1}(\omega)$, $U_{i5}(\omega)$, $U_{i9}(\omega)$ $(i = 1,2,3)$ indicate the voltage output values of any three sensors corresponding to 1, 5 and 9 points.

The derivation of Eq. (33) yields the calibration matrix $\widetilde{\mathbf{V}}(\omega)$ of any three sensors:

$$\widetilde{\mathbf{V}}(\omega) = \mathbf{U}(\omega)[\mathbf{CF}(\omega)]^{-1} \tag{34}$$

The $\widetilde{\mathbf{V}}(\omega)$ calculated from any three selected sensors can be used to initialize the candidate set $\widetilde{\mathbf{V}}\text{cs}(\omega)$. And the three optimal sensors can be obtained by the above D-optimal designs. Finally, point 3, 6, and 7 is the best sensor combination. Subsequently, by substituting the output data of these three sensors into Eq. (20)–(29), a more accurate expression for disturbance force can be obtained.

Next, the improvement of the selection method of the initial set of $\widetilde{\mathbf{V}}\text{cs}(\omega)$ and the improvement of the selection of the sensor order when using D optimization need to be verified.

Fig. 13(a) shows the response RMS values of each sensor when the equipment is installed at positions 2–7 and impacted at point 5 (Position 2–7.5). From this, it can be clearly observed that the optimal three positions of sensors are close to where the vibration source is installed. Besides, the quality of the spectrum response curve is not the same for sensors at different locations from Fig. 13(b).

With the above analysis, the following improvements in D-optimization can be verified:

(1) The initial set of $\widetilde{\mathbf{V}}\mathrm{cs}(\omega)$ is selected by replacing the arbitrary selection with sensors that are closer to the center of mass of the vibration source.
(2) Replace the random selection in sequential exchange algorithms mentioned above with a selection according to the distance from the vibration source.

As seen in Table 1, the average times of optimization among the method using the traversal had been compared, the method using the unimproved D optimization, and the method using the improved D optimization in sensor selection, and the calculation using the improved D optimization was significantly less.

4.3. Dynamic precision test

Finally, the dynamic precision based on the relative error of the platform using the optimal sensor combination is tested. The installation position of the equipment is the same as Fig. 10.

The equipment is installed at positions 2–7 and impacted at point 6 (Position 2–7.6) with hammer. Fig. 14 is the comparison diagrams of measured forces with input generalized forces at position 2–7.6, where (a) is a comparative graph about F_z, (b) is a comparative graph about M_y. The sensitivity and load capacity of the system in this paper are mainly determined by sensors, whose sensitivity can reach −3.8 pC/N, and the maximum load can reach 416 kN (26 kN × 16 = 416 kN).

The dynamic test errors of the three components can be obtained by comparing the equivalent input excitation with the test results. The relative error is calculated from:

$$\boldsymbol{\xi}_i(\omega_j) = \frac{|F_{\mathrm{obi}}(\omega_j)| - |F_i(\omega_j)|}{|F_i(\omega_j)|} \times 100\%, \left(i = 1,2,3; j = 1,2\cdots n_{\mathrm{fft}}\right) \tag{35}$$

where $F_i(\omega_j)$ and $F_{\mathrm{obi}}(\omega_j)$ are both frequency domain complex matrices. To obtain the relative error, both $F_i(\omega_j)$ and $F_{\mathrm{obi}}(\omega_j)$ use the magnitude of each element, where i represents the three components of the generalized force, and j is the element number of the matrix, which represents different frequencies. An error analysis of the three components of the disturbance force in each band allows comparison to be made between the actual values and the test results (see Table 2). The dynamic relative error is mostly within 3% for all three components in the 8–800 Hz range.

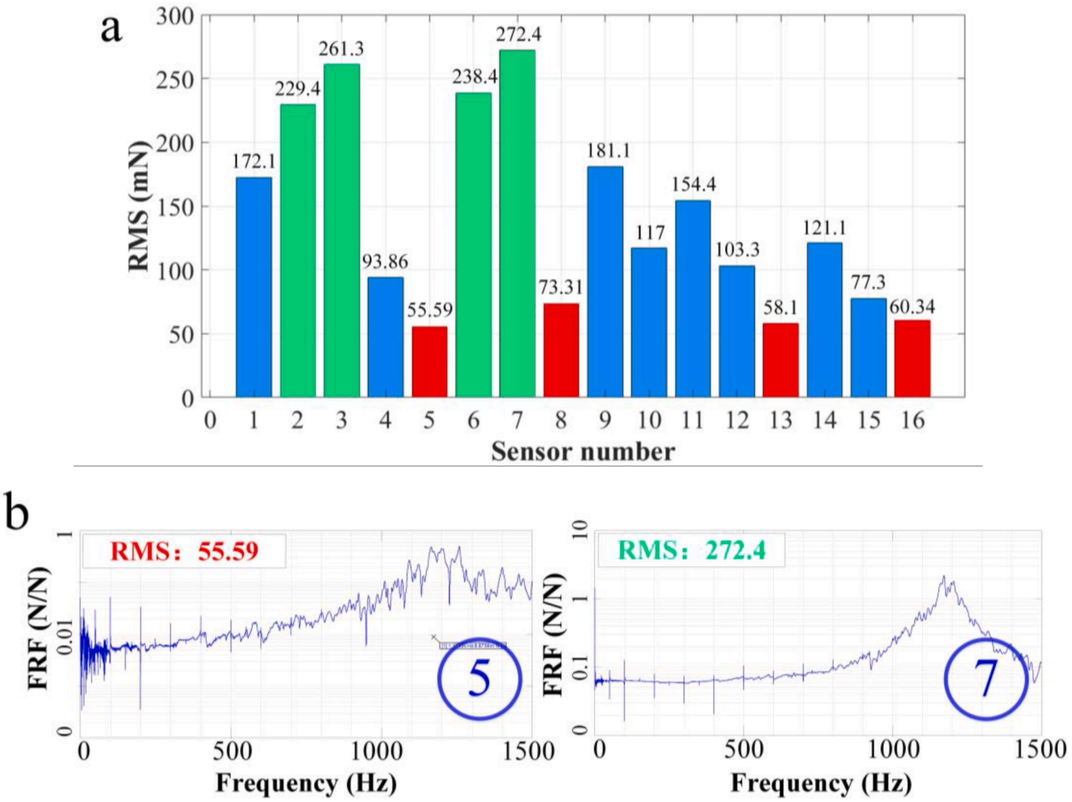

Fig. 13. RMS value of each sensor and spectrum response curve under impact input at position 2–7.5: (a): RMS value; (b): spectrum response curve of point 5 and 7.

Table 1
Comparison of the average number of times for different methods.

Methods	Traversal	Unimproved D optimization	Improved D optimization
Average times (s)	560	32	5

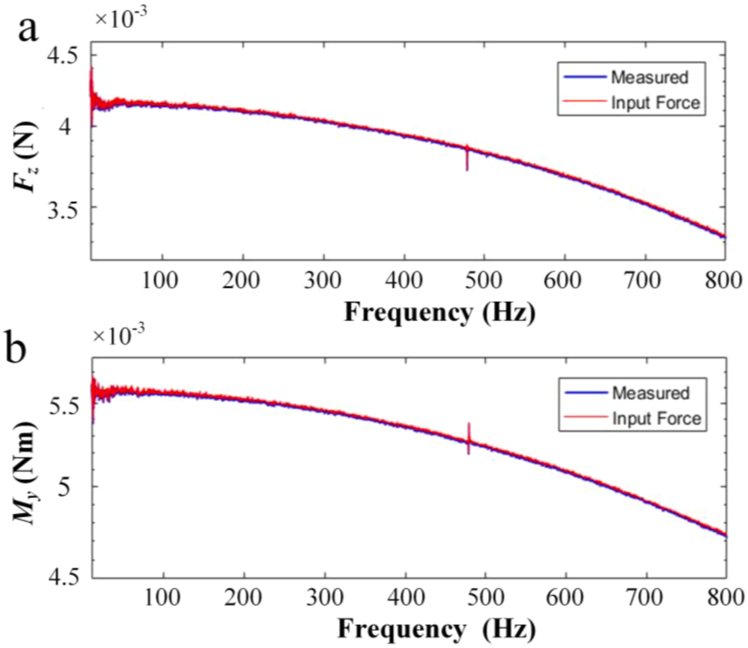

Fig. 14. Comparison of measured forces with input generalized forces under position 2–7.6: (a) F_z; (b) M_y.

According to the above test results, compared with the traditional systems, the measurement precision of the new system has been significantly improved: In the measurement of large-mass vibration source, the change of stiffness of the traditional system is more obvious, as shown in the green box in Fig. 15(a), which will cause the distortion of the original calibration matrix at high-frequency [23]. However, The stiffness of array measurement system in this paper increases significantly when the size of the platform is the same, and the validity of the calibration matrix will be guaranteed to a certain extent, as shown in Fig. 14; Meanwhile, the new system adopts the optimal strategy for different vibration sources measurement, which can eliminate sensors that are not sensitive to the measured source. Relatively, the traditional systems always retain insensitive sensors data. The decoupling process will cause significant loss of measurement precision, as shown in the green box in Fig. 15(b). Compared to Fig. 14, there are significant drift and Signal to Noise Ratio (SNR) reduction in the decoupled signal (Measured force in Fig. 15). Avoiding the situation in Fig. 15 that often occurs in traditional system is also the advantage of the array measurement system and its algorithm.

In addition, the actual in-orbit vibration source disturbance is simulated through a six-dimensional disturbance simulator [37] to examine the precision of the platform under multi-frequency sinusoidal excitation. The test system is shown in Fig. 16. The simulator is mounted on the load platform of the test system through the tooling and the target disturbance force output of the lower platform of the simulator is achieved through closed-loop control (relative error of the simulator is within 3.33%).

In the Fig. 17 a1, b1 and c1, the disturbance outputs (M_x, M_y, F_z) of the in-orbit CMG and cryocooler are simulated, where 46.7 Hz, 116.7 Hz, 233 Hz are the CMG disturbance frequencies, 80 Hz, 160 Hz, 240 Hz are the cryocooler disturbance frequencies, and the 8 Hz excitation is to detect the low frequency characteristics of the system. The low excitation magnitudes in a1, b1, and c1 and the limitations of the simulator's precision make it possible to introduce interference frequencies in the test. Therefore, as shown in Fig. 17 a2, b2 and c2, the excitation magnitude on the basis of a1, b1 and c1 is increased to detect the linearity of the system under different amplitude perturbations, and it can be observed that the interference frequency introduced is significantly reduced after increasing the magnitude of excitation. The data in the Fig. 17 are summarized in the Table 3.

As can be seen from the above table, the difference between the measured value and the input value at 8 Hz is large due to the poor low frequency characteristics of the piezoelectric ceramic, and the measurement precision at the rest of the frequency is high. The relative error of the test system is within 5% and the linear characteristics are stable, and these meet the initial design requirements.

5. Conclusion

This paper has described the analysis, design and testing of a dynamic force measurement system based on an array sensor for large

Table 2
Dynamic relative measurement errors in the 8–800 Hz range.

Frequency range	Relative error (%)		
	F_z	M_x	M_y
8–50 Hz	1.58	1.34	2.21
50–100 Hz	2.23	1.57	1.41
100–150 Hz	1.25	1.68	2.11
150–200 Hz	1.15	1.78	1.89
200–250 Hz	1.36	1.47	1.58
250–300 Hz	0.99	1.18	1.27
300–350 Hz	0.87	1.12	0.86
350–400 Hz	0.68	1.07	0.78
400–450 Hz	0.78	0.68	1.08
450–500 Hz	0.65	0.70	0.87
500–550 Hz	1.37	0.88	1.25
550–600 Hz	1.25	0.91	0.96
600–650 Hz	0.98	1.11	1.26
650–700 Hz	0.78	1.89	1.37
700–750 Hz	1.58	1.75	1.72
750–800 Hz	2.11	1.98	1.80

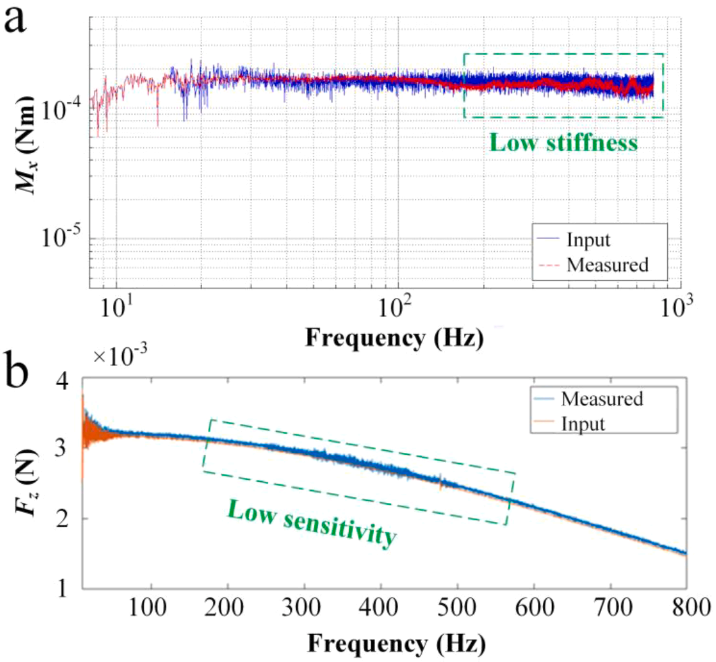

Fig. 15. Disadvantages of traditional measurement systems and their decoupling algorithms: (a) Insufficient stiffness of the system [23]; (b) Loss of measurement precision.

moving devices in spacecraft. The system uses an array of piezoelectric sensors to increase its platform size, stiffness and load capacity, while the precision is improved through use of an efficient optimization algorithm based on pre-vibration. The experimental results obtained from the system prototype show that the system guarantees a high load capacity and high stiffness (fundamental frequency: 1174 Hz; load capacity: 416 kN; dynamic linearity: less than 0.1% full scale (FS)). The dynamic precision in the 8–800 Hz range can reach less than 3% for the 3D generalized force in the force hammer test and the relative error of the test system under sinusoidal excitation is within 5%, which confirmed the feasibility of the array measurement in the vibration source ground test.

CRediT authorship contribution statement

Mingyi Xia: Conceptualization, Formal analysis, Writing – original draft. **Chengbo Zhou:** Investigation, Formal analysis, Writing – original draft. **Enyang Zhang:** Investigation. **Chunyang Han:** Formal analysis, Writing – original draft. **Zhenbang Xu:** Conceptualization, Formal analysis.

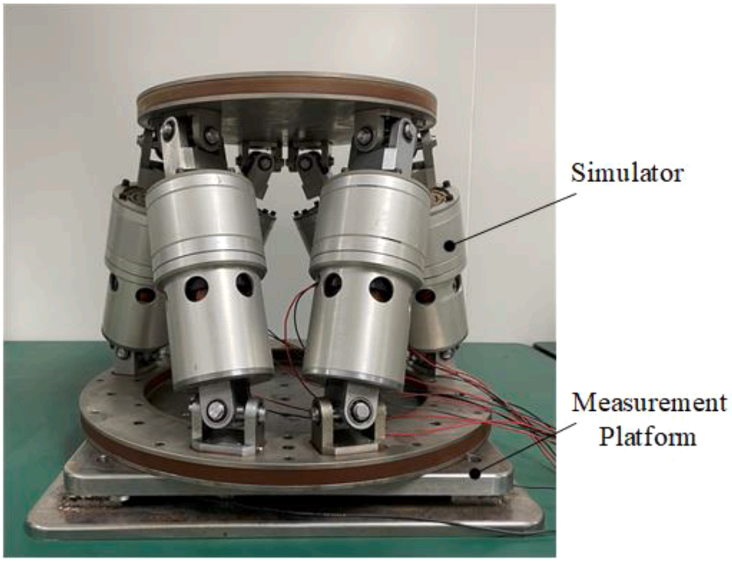

Fig. 16. Test system with simulator.

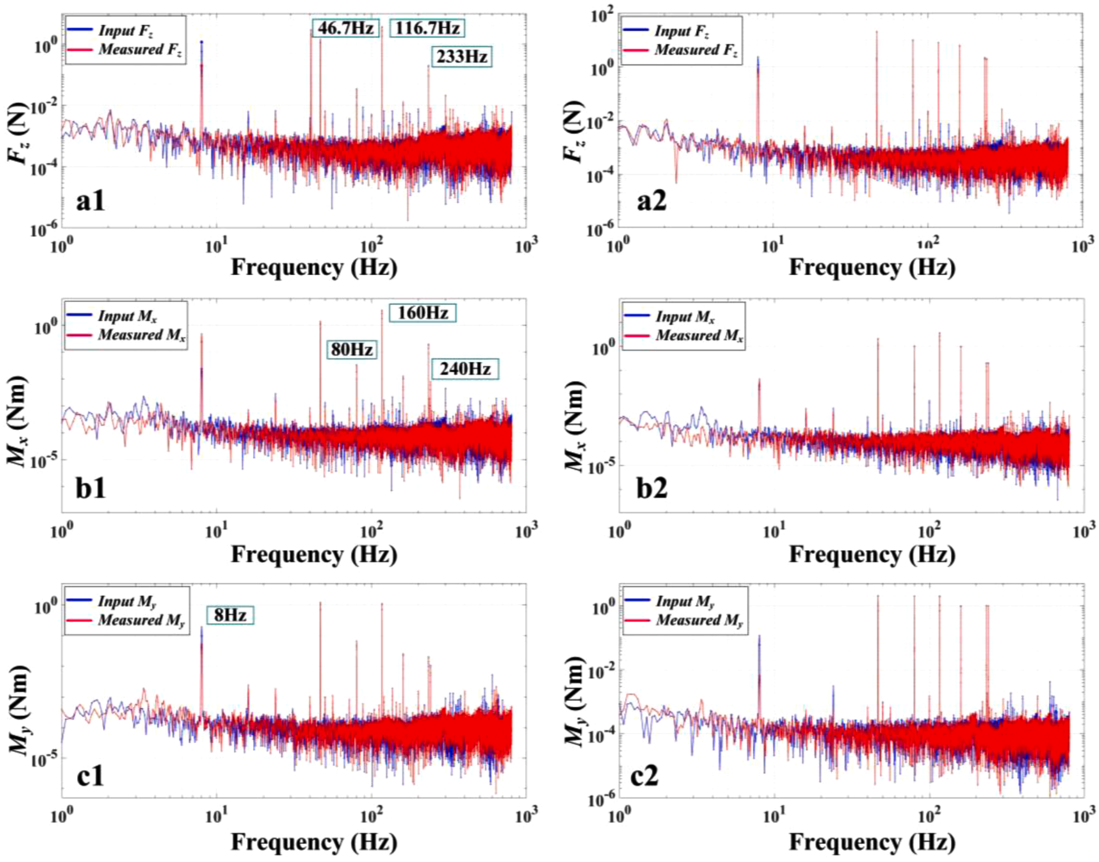

Fig. 17. Comparison of the input force generated by the simulator and the force measured by the platform.

Table 3
Data of the input force generated by the simulator and the measured force at different magnitudes.

Frequency (Hz)		8	46.7	80	116.7	160	233	240
F_z (N)	a1-Input	1.125	2.81	0.35	0.81	0.25	2.5	0.021
	a1-Measured	0.18	2.93	0.34	0.78	0.26	2.21	0.031
	a2-Input	2.368	20	10	8	6	2	2
	a2-Measured	0.86	20.8	9.79	8.05	6.2	2.12	1.88
M_x (Nm)	b1-Input	0.48	1.41	0.034	3.5	0.01	0.2	0.008
	b1-Measured	0.024	1.38	0.03	3.68	0.013	0.18	0.008
	b2-Input	0.042	2	1	3.5	1	0.2	0.2
	b2-Measured	0.031	2.1	1.03	3.65	0.91	0.19	0.19
M_y (Nm)	c1-Input	0.192	1.13	0.065	1.1	0.025	0.02	0.011
	c1-Measured	0.052	1.13	0.066	1.08	0.023	0.018	0.009
	c2-Input	0.12	2	2	2	1	1	1
	c2-Measured	0.0066	2.08	1.97	1.88	0.92	1.02	1.01

Declaration of Competing Interest

None.

Funding

This work was supported by the National Natural Science Foundation of China (No. 11672290) and Jilin Scientific and Technological Development Program (No. 20200404204YY).

References

[1] D. Addari, G.S. Aglietti, M. Remedia, Experimental and numerical investigation of coupled microvibration dynamics for satellite reaction wheels, J. Sound Vib. 386 (2016) 225–241.
[2] R. Masterson, D.W. Miller, R.L. Grogan, Development and validation of reaction wheel disturbance models: empirical model, J. Sound Vib. 249 (3) (2002) 575–598.
[3] C. Liu, X. Jing, S. Daley, F. Li, Recent advances in micro-vibration isolation, Mech. Syst. Signal Process. 56 (2015) 55–80.
[4] P.Y. Bely, The Design and Construction of Large Optical Telescopes, Springer-Verlag, New York, 2003.
[5] H. Wang, Q. Han, D. Zhou, Nonlinear dynamic modeling of rotor system supported by angular contact ball bearings, Mech. Syst. Signal Process. 85 (2017) 16–40.
[6] A.J. Bronowicki, Vibration isolator for large space telescopes, J. Spacecr. Rocket. 43 (2006) 45–53.
[7] H. Wang, Q. Han, D. Zhou, Output torque modeling of control moment gyros considering rolling element bearing induced disturbances, Mech. Syst. Signal Process. 115 (2019) 188–212.
[8] A. Stabile, G.S. Aglietti, G. Richardson, G. Smet, Design and verification of a negative resistance electromagnetic shunt damper for spacecraft micro-vibration, J. Sound Vib. 386 (2017) 38–49.
[9] B.J. Kawak, Development of a low-cost, low micro-vibration CMG for small agile satellite applications, Acta Astronaut. 131 (2017) 113–122.
[10] ECSS-E-HB-32-26A, Spacecraft Mechanical Loads Analysis Handbook, ESA Requirements and Standards Division, 2013.
[11] L. Li, L. Tan, L. Kong, D. Wang, H. Yang, The influence of flywheel micro vibration on space camera and vibration suppression, Mech. Syst. Signal Process. 100 (2018) 360–370.
[12] Y. Sun, Y. Liu, T. Zou, et al., Design and optimization of a novel six-axis force/torque sensor for space robot, Measurement 65 (2015) 135–148.
[13] Q. Liang, D. Zhang, Q. Song, et al., Design and fabrication of a six-dimensional wrist force/torque sensor based on E-type membranes compared to cross beams, Measurement 43 (10) (2010) 1702–1719.
[14] J.W. Joo, K.S. Na, D.I. Kang, Design and evaluation of a six-component load cell, Measurement 32 (32) (2002) 125–133.
[15] L.P. Chao, K.T. Chen, Shape optimal design and force sensitivity evaluation of six-axis force sensors, Sens. Actuators A 63 (2) (1997) 105–112.
[16] S.A. Liu, H.L. Tzo, A novel six-component force sensor of good measurement isotropy and sensitivities, Sens. Actuators A 100 (2) (2002) 223–230.
[17] G.S. Kim, H.J. Shin, J. Yoon, Development of 6-axis force/moment sensor for a humanoid robot's intelligent foot, Sens. Actuators A 141 (2) (2008) 276–281.
[18] Y. Lu, Y. Wang, N. Ye, et al., Development of a novel sensor for hybrid hand with three fingers and analysis of its measure performances, Mech. Syst. Signal Process. 83 (2016) 116–129.
[19] Z.Y. Jia, S. Lin, W. Liu, Measurement method of six-axis load sharing based on the Stewart platform, Measurement 43 (3) (2010) 329–335.
[20] Y. Hou, D. Zeng, J. Yao, et al., Optimal design of a hyperstatic Stewart platform-based force/torque sensor with genetic algorithms, Mechatronics 19 (2) (2009) 199–204.
[21] R. Ranganath, P.S. Nair, T.S. Mruthyunjaya, et al., A force–torque sensor based on a Stewart platform in a near-singular configuration, Mech. Mach. Theory 39 (9) (2004) 971–998.
[22] Y.J. Li, B.Y. Sun, J. Zhang, et al., A novel parallel piezoelectric six-axis heavy force/torque sensor, Measurement 42 (5) (2009) 730–736.
[23] M.Y. Xia, Z.B. Xu, K. Han, Q. Huo, A. Li, Dynamic disturbance force measurement platform for large moving device in spacecraft, J. Sound Vib. 447 (2019) 61–77, https://doi.org/10.1016/j.jsv.2019.01.053.
[24] Y.J. Li, G.C. Wang, D. Zhao, X. Sun, Q.H. Fang, Research on a novel parallel spoke piezoelectric 6-DOF heavy force/torque sensor, Mech. Syst. Signal Process. 36 (1) (2013) 152–167.
[25] R. Liang, Q.M. Wang, High sensitivity piezoelectric sensors using flexible PZT thick-film for shock tube pressure testing, Sens. Actuators A 235 (2015) 317–327.
[26] D. Durand, C. France, Measurement sensor for a linking wrench between two mechanical parts, as well as its manufacturing process: US, US005821431A[P/OL], 1998.
[27] Y. Sujan, G. Uma, M. Umapathy, Design and testing of piezoelectric resonant pressure sensor, Sens. Actuators A 250 (2016) 177–186.
[28] M.Y. Xia, C. Qin, X.M. Wang, et al., Modeling and experimental study of dynamic characteristics of the moment wheel assembly based on structural coupling, Mech. Syst. Signal Process. 146 (2021), 107007, https://doi.org/10.1016/j.ymssp.2020.107007.
[29] Q. Luo, L. Tong, Design and testing for shape control of piezoelectric structures using topology optimization, Eng. Struct. 97 (2015) 90–104.
[30] Y.J. Li, J. Zhang, Z.Y. Jia, et al., Research on force-sensing element's spatial arrangement of piezoelectric six-component force/torque sensor, Mech. Syst. Signal Process. 23 (8) (2009) 2687–2698.

[31] J.P. Chen, C. Wei, M.Y. Xia, An ultra-low frequency micro-vibration testing platform based on strain-resistance effect, J. Vib. Shock 24 (33) (2014) 77–81.

[32] L. Ye, M. Yang, L. Xu, et al., Optimization of inductive angle sensor using response surface methodology and finite element method, Measurement 48 (1) (2014) 252–262.

[33] B. Wu, J. Luo, F. Shen, et al., Optimum design method of multi-axis force sensor integrated in humanoid robot foot system, Measurement 44 (9) (2011) 1651–1660.

[34] D.K. Gupta, A.K. Dhingra, Dynamic programming approach to load estimation using optimal sensor placement and model reduction, Int. J. Comput. Methods 15 (3) (2017), 1850071.

[35] D.K. Gupta, A.K. Dhingra, A reduced modal parameter based algorithm to estimate excitation forces from optimally placed accelerometers, Inverse Probl. Sci. Eng. 25 (3) (2017) 397–417.

[36] D.K. Gupta, A.K. Dhingra, Input load identification from optimally placed strain gages using D-optimal design and model reduction, Mech. Syst. Signal Process. 40 (2) (2013) 556–570.

[37] X. Wang, Z. Xu, M. Xia, et al., Research on a six-degree-of-freedom disturbance force and moment simulator for space micro-vibration experiments, J. Sound Vib. 432 (2018) 530–548.